Vol 457|8 January 2009|doi:10.1038/nature07636

LETTERS

# Electrically pumped photonic-crystal terahertz lasers controlled by boundary conditions

Y. Chassagneux[1], R. Colombelli[1], W. Maineult[2], S. Barbieri[2], H. E. Beere[3], D. A. Ritchie[3], S. P. Khanna[4], E. H. Linfield[4] & A. G. Davies[4]

**Semiconductor lasers based on two-dimensional photonic crystals[1,2] generally rely on an optically pumped central area, surrounded by un-pumped, and therefore absorbing, regions[3]. This ideal configuration is lost when photonic-crystal lasers are electrically pumped, which is practically more attractive as an external laser source is not required. In this case, in order to avoid lateral spreading of the electrical current, the device active area must be physically defined by appropriate semiconductor processing. This creates an abrupt change in the complex dielectric constant at the device boundaries, especially in the case of lasers operating in the far-infrared, where the large emission wavelengths impose device thicknesses of several micrometres. Here we show that such abrupt boundary conditions can dramatically influence the operation of electrically pumped photonic-crystal lasers. By demonstrating a general technique to implement reflecting or absorbing boundaries, we produce evidence that whispering-gallery-like modes or true photonic-crystal states can be alternatively excited. We illustrate the power of this technique by fabricating photonic-crystal terahertz (THz) semiconductor lasers, where the photonic crystal is implemented via the sole patterning of the device top metallization. Single-mode laser action is obtained in the 2.55–2.88 THz range, and the emission far field exhibits a small angular divergence, thus providing a solution for the quasi-total lack of directionality typical of THz semiconductor lasers based on metal–metal waveguides[4].**

Terahertz radiation—loosely defined as the region of the electromagnetic spectrum between 0.5 THz and 5 THz (ref. 5)—finds promising applications in very different areas of science and technology, such as astronomy, environmental monitoring and security[6]. However, its spectral location—between optical and microwave frequencies—has hindered the development of compact semiconductor sources. A significant breakthrough in this direction took place in 2002[7] with the demonstration of a quantum cascade laser operating at ~4.4 THz. Quantum cascade lasers rely on transitions between quantized conduction band states of a suitably designed semiconductor multi-quantum-well structure[8]. They are in-plane emitters, with the electric-field vector perpendicular to the plane of the layers, and the unnatural surface emission (often desirable) has to be engineered. The advantage of transverse magnetic polarization, however, is the possibility of exploiting surface plasmons for waveguiding[9]. Indeed, surface-plasmon single-metal[7] and metal–metal[10] ridge waveguides proved to be a key ingredient in the extension of the quantum cascade concept from mid-infrared to long-infrared wavelengths ($\lambda > 19\,\mu m$).

In the mid-infrared, photonic-crystal-based quantum cascade structures have been demonstrated for surface emission[11] and normal-incidence detection[12]. The application of photonic-crystal technology to active devices is particularly appealing because it allows the achievement of simultaneous spectral and spatial (surface emission, beaming and so on) mode engineering. In the above-mentioned mid-infrared structures, the effective index contrast was obtained via a deep etch of the semiconductor material. This approach has been transferred to the THz range to realize devices based on lattices of deeply etched pillars[13,14]. Besides the high degree of technological complexity, these devices did not lead to surface emission, and they did not exploit the possibility of 'printing' the photonic structure on the top metal only. First-order[15] and second-order[16] distributed-feedback devices were demonstrated only recently, with one-dimensional metallic gratings implemented on top of standard ridge-waveguide lasers. At shorter mid-infrared wavelengths and for edge emitting devices, a plasmonic collimator was also recently demonstrated[17].

In this work we demonstrate a new approach to the implementation of a resonator for THz semiconductor lasers, based on a two-dimensional (2D) photonic-crystal structure, lithographically transferred onto the top metallization only of a metal–metal THz quantum cascade laser[18]. In addition, we show that the operation of the photonic crystal is critically dependent on the boundary conditions. This finding is general, and is a key element for the development of any electrically pumped photonic-crystal device. Devices with a similar geometry have been reported in ref. 19. However, the crucial role of boundary conditions was not investigated, and no effect of the photonic crystal on the far-field emission pattern was detected. Our micro-resonators exhibit—when the correct boundary conditions are implemented—lithographically tunable single-mode emission, and an angularly narrow (though not always single-lobed) far-field emission pattern.

The quantum cascade laser used in this work was grown by molecular beam epitaxy in the GaAs/AlGaAs material system. It consists of a 12-μm-thick, bound-to-continuum active region with emission at ~2.7 THz (ref. 20). The active core is sandwiched between 700 nm, $2 \times 10^{18}\,cm^{-3}$ and 80 nm, $5 \times 10^{18}\,cm^{-3}$ doped layers, forming the lower and upper contacts. The quantum cascade wafer was thermo-compressively bonded onto an $n^+$-GaAs wafer. After selective etching of the GaAs substrate, the 700-nm-thick top doped layer was thinned to 200 nm to reduce free carrier absorption. Hexagonal mesas were etched down to the bottom metal to avoid lateral current dispersion, and the photonic-crystal pattern was implemented in the top metallization only, which acts as a contact and—simultaneously—provides the necessary optical feedback. In Fig. 1a a schematic cross-section of a typical device is displayed, and an optical microscope image taken from the top is shown in Fig. 1b.

Two-dimensional photonic-crystal slab waveguide lasers can be divided in two families: defect mode lasers and band-edge mode lasers. The former operate at frequencies inside the bandgap by intentionally introducing a defect that supports localized modes[21]. Band-edge mode

[1]Institut d'Electronique Fondamentale, Université Paris Sud and CNRS, UMR 8622, 91405 Orsay, France. [2]Laboratoire MPQ, Université Paris7 and CNRS, UMR 7162, 75013 Paris, France. [3]Cavendish Laboratory, University of Cambridge, Cambridge CB3 OHE, UK. [4]School of Electronic and Electrical Engineering, University of Leeds, Leeds LS2 9JT, UK.

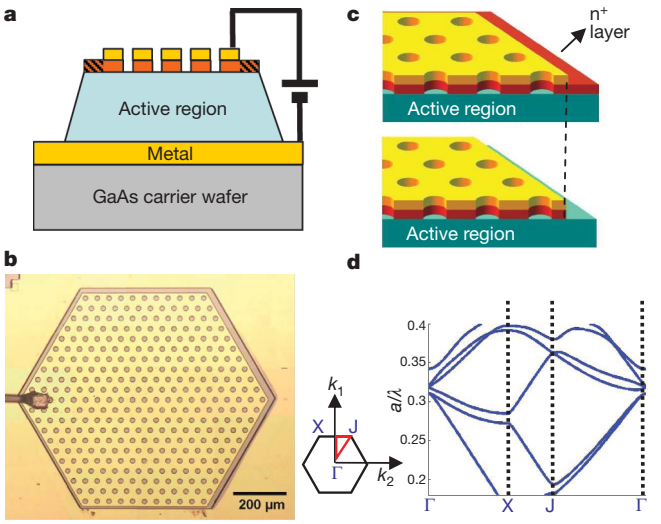


**Figure 1 | Device details and design.** **a**, Schematic cross-section of the device. The laser active region (blue) is sandwiched between two metal Ti/Au contact layers. The top metal is patterned with the desired photonic-crystal design. The top $n^+$-GaAs contact layer, approximately 200 nm thick (red) is removed in the photonic-crystal holes in order to reduce the losses. At the edge of the device, the $n^+$-GaAs layer (red hatched region) can be removed or left in place, if mirror or absorbing boundary conditions, respectively, need to be implemented. **b**, Optical microscope image of the surface of a typical device. The wire bonding is applied directly on the top metallization. **c**, Detailed scheme of the boundary conditions implementation technique. When the top $n^+$ contact, represented as a red layer, is left in place between the metal edge and the mesa periphery (top panel), the absorption is high and the boundary behaves like an absorber. When instead it is removed (bottom panel), the mode mismatch at the metal edge introduces a high reflectivity, and therefore mirror boundary conditions. **d**, Transverse-magnetic photonic band structure (around the point Γ) of the trigonal lattice used for the experiment, for $r/a = 0.22$. The calculation is fully 3D and therefore it does not require an effective index for the holes. The distribution of the electromagnetic field is calculated with a finite-element solver for a single lattice unit cell using Bloch-periodic boundary conditions. $k_1$, $k_2$ indicate axes in reciprocal space.

lasers instead operate in regions of energy–momentum space that have a high photonic density of states and a corresponding small group velocity[22]. We implemented the latter device architecture in order to take advantage of (1) the connected nature of the lattice that greatly simplifies the processing, and (2) the spatial delocalization of band-edge modes[3], which allows for improved power extraction.

It is intuitively clear that the index contrast induced by the top metal patterning originates from the following effect: the guided mode sees two different effective indexes ($n_{\mathrm{eff}}$) as it propagates, the large $n_{\mathrm{eff}}$ of the guided surface-plasmon mode where the metal is left intact, and a lower $n_{\mathrm{eff}}$, corresponding to a more delocalized mode where the metal is removed[18]. However, the photonic-band structure of our devices cannot—in principle—be calculated within a 2D effective-index approximation, as this approach would not take into account the effect of the mode profile in the regions not covered by metal. Therefore we performed 3D photonic-band-structure calculations by solving the Helmholtz equation in a single unit cell of the triangular lattice of Fig. 1, with Bloch periodic boundary conditions applied in the plane. The resulting band structure (Fig. 1d) allows the appropriate photonic-crystal dimensions to be inferred in order to spectrally overlap the material gain with the regions of small group velocity.

We fabricated a series of devices with different photonic-lattice periods ($a$) in order to target the band edge-states at the Γ-point, corresponding to $a/\lambda = 0.33$. We also fabricated devices with different $r/a$ values (where $r$ is the hole radius) for a fixed period $a = 36.5\,\mu\mathrm{m}$ (including a control sample with unpatterned top metallization).

The boundary conditions represent the last crucial point that needs to be addressed for a correct device design. This issue is often overlooked for optically pumped devices[3], as the photonic crystal is usually much larger than the laser excitation spot. Absorbing boundary conditions are therefore naturally implemented, owing to the photonic-crystal regions that are not optically pumped. The case of a current injection device is radically different, because in general the photonic crystal must have a finite size. For metal–metal waveguides in particular, it can be shown that the facet reflectivities are extremely high, as the waveguide thickness is much smaller than the lasing wavelength[23].

In order to tailor the reflectivity at the device boundary, in our photonic-crystal devices the hexagonal etched mesas are slightly larger than the top metallization. The 200-nm-thick top contact layer—which is removed in the photonic-crystal holes to reduce the losses—can be etched or left in place at the mesa periphery (hatched red region in Fig. 1a). If left in place (Fig. 1c, top panel), absorbing boundary conditions are obtained as the loss ($\alpha$) introduced by the $n^{++}$-layer, when not metal-covered, is high ($\alpha \approx 750\,\mathrm{cm}^{-1}$). If instead it is removed (Fig. 1c, bottom panel), mirror boundary conditions are obtained, as exemplified in ref. 24 for micro-disk devices. In this case the losses are at least 50 times lower and equal to $\sim 8\,\mathrm{cm}^{-1}$. Details are given in Supplementary Information. For each photonic-crystal design, pairs of devices have been fabricated: one with mirror boundaries (M) and one with absorbing boundaries (A). In the rest of the paper, these will be labelled as M devices and A devices, respectively.

Figure 2a reports the threshold current density ($J_{\mathrm{th}}$) for a set of M and A devices as a function of $r$, the hole radius of the photonic lattice, with a constant lattice spacing $a = 36.5\,\mu\mathrm{m}$. A markedly different behaviour can be observed for the two device families. All M devices lase at approximately the same $J_{\mathrm{th}}$, $\sim 95 \pm 5\,\mathrm{A\,cm}^{-2}$, which is of the same order as what was obtained on metal–metal ridges fabricated from the same epitaxial material. On the contrary, the $J_{\mathrm{th}}$ of A devices strongly depends on the photonic-crystal characteristics: $J_{\mathrm{th}}$ is maximum for the 'control' sample ($r = 0$) and decreases down to $J_{\mathrm{th}} \approx 110\,\mathrm{A\,cm}^{-2}$ for $r = 8\,\mu\mathrm{m}$ (the $J_{\mathrm{th}}$ increase for $r \geq 10\,\mu\mathrm{m}$ is attributed to device damage when wire-bonding on the top metallization for large values of $r/a$). These results offer an initial indication that different optical modes are active, depending on the applied boundary conditions. M devices, being unaffected by the photonic crystal (Fig. 2a), probably lase on whispering-gallery-like modes[24,25], while devices with absorbing boundaries are our candidates for photonic-crystal lasing on delocalized band-edge states[22]. The spatial overlap between whispering-gallery-like and photonic-crystal modes is ~50% (see Supplementary Information). Mode competition therefore causes mode selection, and the lasing mode is the one with the highest $Q$ factor. When the $n^+$ layer is removed, whispering-gallery-like modes have a high $Q$ factor, and therefore reach lasing before the photonic-crystal modes. When the $n^+$ layer is instead left in place, the $Q$ factor of the whispering-gallery-like modes decreases by approximately a factor of two and the photonic-crystal modes are now favoured.

To elucidate the origin of lasing, we fabricated a second set of devices with several different photonic-lattice spacings $a$, and with $r/a$ fixed at the most favourable value of 0.22. The values of $a$ were chosen around $a/\lambda = 0.33$, to overlap the quantum cascade material gain peak with the band-edge states at point Γ (Fig. 1c). The corresponding light–current–voltage curves for A- and M-device families are shown in Fig. 2b and c, respectively. M devices exhibit identical $J_{\mathrm{th}}$, confirming that they are unaffected by the photonic structure patterned on the top metal. In contrast, the $J_{\mathrm{th}}$ for the devices with absorbing boundary conditions depend on the lattice spacing, and they roughly follow the active material gain curve.

The clear demonstration that a photonic-crystal mode is active when absorbing boundary conditions are applied comes from the spectral analysis. Figure 3a shows the laser spectra of several M

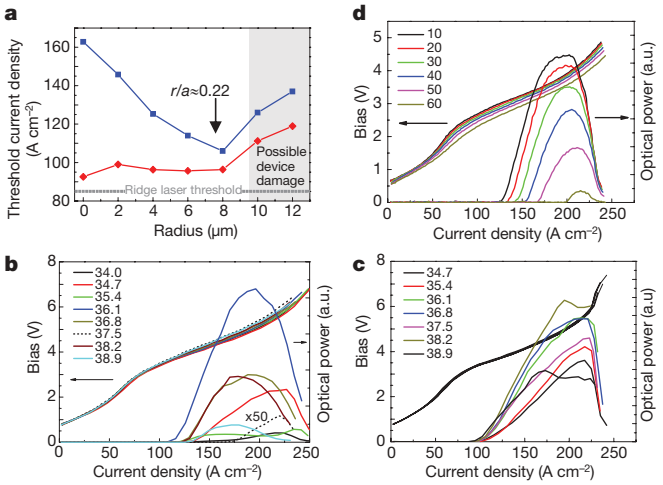


**Figure 2 | Light–current–voltage characteristics and laser thresholds.** **a**, Threshold current density ($T = 10$ K) as a function of the photonic-crystal hole radius ($r$) and constant photonic-lattice spacing $a = 36.5$ μm. Results for devices with absorbing (blue curve) and with mirror (red curve) boundary conditions are shown. A He-cooled Si bolometer was used for detection. **b**, **c**, Light–current-density and voltage–current-density curves as a function of $a$ (shown in key in μm) for a different set of devices with fixed $r/a = 0.22$. The most favourable value of $r/a$ has been chosen, based on the results reported in **a**. Devices with absorbing boundary conditions (A devices) are reported in **b**, while those with mirror boundary conditions (M devices) are shown in **c**. The A device with $a = 37.5$ μm is probably damaged (dashed line in **b**), since its output power is 50 times reduced with respect to the others. The M devices exhibit identical $J_{th}$, confirming that they are unaffected by the photonic-structure patterned on the top metal, contrary to the A devices. The threshold densities are calculated as follows: when the $n^+$ layer is present, the whole disk surface is employed, and when the $n^+$ layer is missing, the metal contact surface only is employed, since the top $n^+$ layer is responsible for current spreading. Data in **b** and **c** justify this choice *a posteriori*: the voltage–current characteristics plotted in current-density perfectly overlap for the whole set of devices. **d**, Light–current–voltage characteristics (20-kHz repetition rate, 300-ns pulse width) as a function of temperature (shown in key in K) for a typical photonic-crystal (A) device. The maximum operating temperature ($T_{max}$) is 62 K, just 15 K lower than standard ridge waveguides fabricated from the same material. $T_{max}$ in continuous wave is 44 K (data not shown).

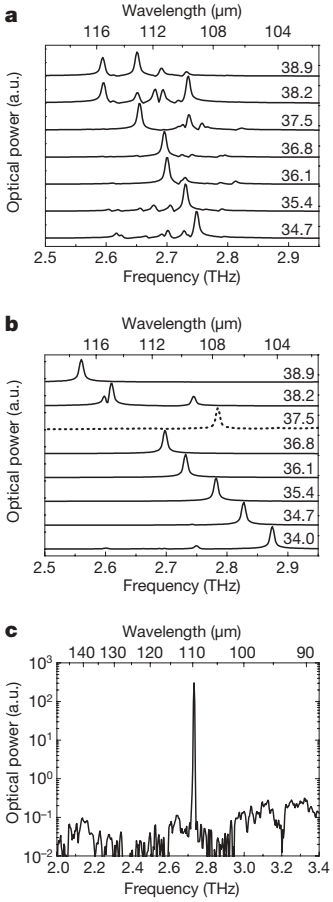


**Figure 3 | Spectral characterizations.** Laser output spectra for several devices with different photonic-lattice periods, $a$ (shown next to the spectra, in μm). **a**, Devices with mirror boundary conditions; **b**, identical devices with absorbing boundary conditions. In the first case the emission is multimode, while in the second case the spectra clean up, become mostly single-mode, and exhibit a clear frequency shift with $a$. The device with $a = 37.5$ μm in **b** is anomalous, and is probably damaged; its output power is in fact 50 times less than the others (see dashed curve in Fig. 2b). The spectra were acquired in rapid scan mode with a resolution of 0.125 cm$^{-1}$ using a Bruker IFS66 FTIR and a He-cooled Si-bolometer detector. **c**, Typical single-mode spectrum of a photonic-crystal (A) device with $a = 36.1$ μm, on a log-linear scale. A side-mode suppression ratio of at least 30 dB is obtained.

devices as a function of the photonic-lattice spacing. The emission is multimode, and no clear trend with the photonic-crystal characteristic is observed. In contrast, when absorbing boundary conditions are implemented on identical devices, the spectra dramatically clean up (Fig. 3b): almost all the devices become single mode, and the emission is lithographically tuned between 2.55 THz and 2.88 THz ($\lambda \approx 104 \rightarrow 118$ μm). Single-mode devices show a sideband suppression ratio of more than 30 dB (Fig. 3c), and the typical maximum operating temperature is 60 K (Fig. 2d). These characteristics, together with the continuous-wave operation data (not shown) prove that this technology is viable for applications.

We have established that controlling the boundary conditions allows the device to be operated on the desired mode. We will now show the effect of this mode selection on the far-field emission patterns. Figure 4b–h reports several experimental far fields obtained by scanning a Golay cell detector at constant distance from the lasers (Fig. 4a defines the angles of scanning). Figure 4b shows the results for a control device: the emission is non-directional, as expected since no top-metal patterning is present. Figure 4c and d refers instead to two different photonic-crystal devices with mirror boundary conditions. The emission is non-directional in these cases also, and several hot spots are present. These devices exhibit the same problems, typical of standard metal–metal waveguides[4]. When absorbing boundary conditions are introduced, the far fields dramatically localize in the angular domain (Fig. 4e–h). The angular patterns are mostly bi-lobed, with one lobe typically dominant. Each lobe is angularly very narrow, $\leq 10^\circ$, evidence that the laser mode is spatially more delocalized.

To elucidate the role of the wire bonding (applied directly to the device surface), we performed a series of tests. Figure 4e and f correspond to the same device, bonded first on the periphery (Fig. 4e), then re-bonded in the centre (Fig. 4f). The far fields are very similar, proving that the bonding is not directly involved in the surface emission process. Figure 4g and h corresponds instead to two different devices, wire-bonded in the centre and on all the resonator corners, respectively. The latter device exhibits a single, angularly extremely narrow lobe at ($\varphi \approx 10^\circ$, $\theta \approx -10^\circ$). The former device shows instead a multi-lobed emission, with two dominant lobes, allowing us to propose a hypothesis to explain the device behaviour. The far-field emission pattern is multi-lobed, as observed in band-edge lasers operating at shorter wavelengths[11], but the position of the metallic wire-bondings—and possible device imperfections—affects the slowly varying components of the device near field. As shown in ref. 26, minute modifications of a photonic-crystal device near-field can yield important far-field changes. As a result of the bonding, the symmetry is broken and one—or more—lobe is enhanced or suppressed. A full understanding of the laser near-field requires 3D finite-difference time-domain (FDTD) simulations which are beyond the

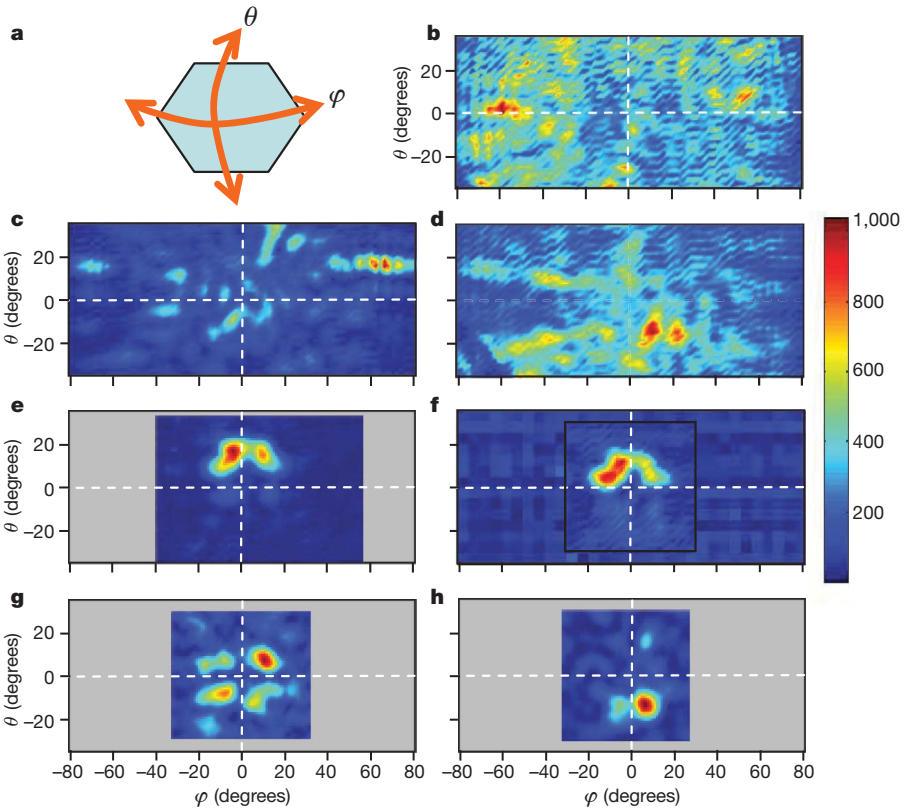


**Figure 4 | Far-field characterizations.** Far-field emission patterns of several devices, obtained by scanning a Golay cell at a distance of 6 cm or 13 cm from the surface of the device. A pinhole of 2 mm in diameter was used to partially shield the detector active element. **a**, Device position and definitions of the angles $\varphi$ and $\theta$. **b**, Far field of a 'control' device, that is, a cavity with no holes in the top metallization and mirror boundary conditions. The emission is non-directional, and it extends up to very large angles of ~80°. **c**, Far field of a device with mirror boundary conditions (an M device), with $a = 36.8$ μm and $r/a = 0.22$. (See Fig. 3a for the emission spectrum of this device.) The emission is not directional, and a hot spot is present at a very large $\varphi$ value of ~80°. We believe it might originate from a mesa facet. **d**, Far field of another M device, with $a = 35.4$ μm and $r/a = 0.22$. (See Fig. 3a for the spectrum of this device.) The emission is highly non-directional, with several hot spots distributed in a very wide angular range. **e**, Far field of a device with absorbing boundary conditions (an A device), with $a = 35.4$ μm and $r/a = 0.22$ (Fig. 3b for the spectrum of this device). Compared with the M devices, the emission dramatically cleans up. It becomes highly directional, with two lobes concentrated in a narrow angular range (±10°). The bonding wire is in this case applied to the top left edge of the device. **f**, Far field of the same device shown in **e**, after the bonding wire is removed from the edge and re-applied in the centre of the device. The far-field is very similar to **e**, suggesting that the bonding is not directly involved in the emission process. The black continuous line marks the region that has been scanned at higher angular resolution. **g**, Far field of an A device, with $a = 35.4$ μm and $r/a = 0.22$ (Fig. 3b for the spectrum of this device), and bonding wire applied in the centre of the device. The emission exhibits four lobes (two of them dominant with respect to the others), within an angular range of ~20°×30°. **h**, Far field of another A device, with $a = 36.1$ μm and $r/a = 0.22$ (Fig. 3b for the spectrum of this device), and bonding wires applied at all the six edges of the hexagon. These measurements show that (1) when absorbing boundary conditions are implemented, the system lases on a delocalized photonic-crystal mode, and as a consequence the emission far-field pattern localizes in the angular domain; and (2) the bonding wires are not direct emission sources, rather their presence affects the slowly varying components of the device near field, thus enhancing/suppressing some of the lobes.

scope of this paper. However, initial very encouraging results based on 2D FDTD simulations are reported in the Supplementary Information. With new, better fabricated and more powerful devices, we obtain in fact an unambiguous identification of lasing on the hexapolar and monopolar Γ-point band-edge states (data shown in Supplementary Information).

In conclusion, we have shown that boundary conditions are a key parameter for the effective design and implementation of active, electrically injected photonic devices. The application of this idea to a class of semiconductor THz lasers where the photonic-crystal structure has been 'written' in the top metallization layer yielded lithographically tunable, single-mode operation and—simultaneously—angularly narrow surface emission. The addition of these functionalities comes at almost no detriment to the overall device performance. This demonstration represents an important step in the development of photonic-crystal micro-cavity lasers for practical applications. The remaining issues, namely the increase in output power and full control of the emission far field, can be addressed by using a thin top metallization layer[27], and by using more advanced photonic-crystal designs, such as graded photonic structures[28]. Finally, a similar approach could be used to explore systems not only in the weak-coupling regime (lasing), but also active devices in the strong-coupling regime (intersubband polaritons)[29]. In the THz range particularly, where a novel ultrastrong-coupling regime is expected to arise[30], the possibility of accurately tuning the frequency position of the photonic-crystal cavity resonance is a valuable experimental tool.

**Received 29 March; accepted 5 November 2008.**

1. Yablonovitch, E. Inhibited spontaneous emission in solid-state physics and electronics. *Phys. Rev. Lett.* **58**, 2059–2062 (1987).
2. Sajeev, J. Strong localization of photons in certain disordered dielectric superlattices. *Phys. Rev. Lett.* **58**, 2486–2489 (1987).
3. Letartre, X., Monat, C., Seassal, C. & Viktorovitch, P. Analytical modeling and an experimental investigation of two-dimensional photonic crystal microlasers: Defect state (microcavity) versus band-edge state (distributed feedback) structures. *J. Opt. Soc. Am. B* **22**, 2581–2595 (2005).
4. Adam, A. J. L. *et al.* Beam pattern of terahertz quantum cascade lasers with subwavelength cavity dimensions. *Appl. Phys. Lett.* **88**, 151105 (2006).
5. Sakai, K. *Terahertz Optoelectronics* (Topics in Applied Physics, Vol. 97, Springer, 2005).
6. Mittleman, D. *Sensing with Terahertz Radiation* (Springer Series in Optical Sciences, Vol. 85, Springer, 2004).

7. Kohler, R. *et al.* Terahertz semiconductor-heterostructure laser. *Nature* **417,** 156–159 (2002).
8. Williams, B. S. Terahertz quantum-cascade lasers. *Nature Photon.* **1,** 517–525 (2007).
9. Sirtori, C. *et al.* Long-wavelength ($\lambda = 8$–$11.5\ \mu m$) semiconductor lasers with waveguides based on surface plasmons. *Opt. Lett.* **23,** 1366–1368 (1998).
10. Unterrainer, K. *et al.* Quantum cascade lasers with double metal-semiconductor waveguide resonators. *Appl. Phys. Lett.* **80,** 3060–3062 (2002).
11. Colombelli, R. *et al.* Quantum cascade surface-emitting photonic crystal laser. *Science* **302,** 1374–1377 (2003).
12. Schartner, S. *et al.* Band structure mapping of photonic crystal intersubband detectors. *Appl. Phys. Lett.* **89,** 151107 (2006).
13. Dunbar, L. A. *et al.* Design, fabrication and optical characterization of quantum cascade lasers at terahertz frequencies using photonic crystal reflectors. *Opt. Express* **13,** 8960–8968 (2005).
14. Zhang, H., Dunbar, A., Scalari, G., Houdré, R. & Faist, J. Terahertz photonic crystal quantum cascade lasers. *Opt. Express* **15,** 16818–16827 (2007).
15. Mahler, L. *et al.* High-performance operation of single-mode terahertz quantum cascade lasers with metallic gratings. *Appl. Phys. Lett.* **87,** 181101 (2005).
16. Kumar, S., Williams, B. S., Qin, Q., Lee, A. W. M. & Hu, Q. Surface-emitting distributed feedback terahertz quantum-cascade lasers in metal-metal waveguides. *Opt. Express* **15,** 113–128 (2007).
17. Yu, N. *et al.* Small-divergence semiconductor lasers by plasmonic collimation. *Nature Photon.* **2,** 564–570 (2008).
18. Bahriz, M., Moreau, V., Colombelli, R., Crisafulli, O. & Painter, O. Design of mid-IR and THz quantum cascade laser cavities with complete TM photonic bandgap. *Opt. Express* **15,** 5948–5965 (2007).
19. Sirigu, L. *et al.* Terahertz quantum cascade lasers based on two-dimensional photonic crystal resonators. *Opt. Express* **16,** 5206–5217 (2008).
20. Barbieri, S. *et al.* 2.9 THz quantum cascade lasers operating up to 70 K in continuous wave. *Appl. Phys. Lett.* **85,** 1674–1676 (2004).
21. Painter, O. *et al.* Two-dimensional photonic band-gap defect mode laser. *Science* **284,** 1819–1821 (1999).
22. Sakai, K., Miyai, E. & Noda, S. Two dimensional coupled wave theory for square-lattice photonic-crystal lasers with TM-polarization. *Opt. Express* **15,** 3981–3990 (2007).
23. Kohen, S., Williams, B. S. & Hu, Q. Electromagnetic modeling of terahertz quantum cascade laser waveguides and resonators. *J. Appl. Phys.* **97,** 053106 (2005).
24. Chassagneux, Y. *et al.* Terahertz microcavity lasers with subwavelength mode volumes and thresholds in the milliampere range. *Appl. Phys. Lett.* **90,** 091113 (2007).
25. Wiersig, J. Hexagonal dielectric resonators and microcrystal lasers. *Phys. Rev. A* **67,** 023807 (2003).
26. Kim, S.-H., Kim, S.-K. & Lee, Y.-H. Vertical beaming of wavelength-scale photonic crystal resonators. *Phys. Rev. B* **73,** 235117 (2006).
27. Vuckovic, J., Loncar, M. & Scherer, A. Surface plasmon enhanced light-emitting diode. *IEEE J. Quant. Electron.* **36,** 1131–1144 (2000).
28. Srinivasan, K. & Painter, O. Momentum space design of high-Q photonic crystal optical cavities. *Opt. Express* **10,** 670–684 (2002).
29. Colombelli, R., Ciuti, C., Chassagneux, Y. & Sirtori, C. Quantum cascade intersubband polariton light emitters. *Semicond. Sci. Technol.* **20,** 985–990 (2005).
30. Ciuti, C. & Carusotto, I. On the ultrastrong vacuum Rabi coupling of an intersubband transition in a semiconductor microcavity. *J. Appl. Phys.* **101,** 081709 (2007).


**Supplementary Information** is linked to the online version of the paper at www.nature.com/nature.

**Acknowledgements** We thank J.-M. Lourtioz, F. Julien, C. Sirtori, L. Sirigu, G. Scalari and V. Moreau for discussions, P. Gellie for technical help, and J. Alton for the Golay cell. Device fabrication was performed at the CTU-IEF-Minerve, which was partially funded by the Conseil Général de l'Essonne. This work was conducted as part of a EURYI scheme award (www.esf.org/euryi).

**Author Information** Reprints and permissions information is available at www.nature.com/reprints. Correspondence and requests for materials should be addressed to R.C. (raffaele.colombelli@u-psud.fr).